Calculation of PSF Factors and Solid Angles for ISOPHOT

Bernhard Schulz

ISO Data Centre, Astrophysics Division of ESA, Villafranca, Spain

22 November 2000, Version 1.0,
SAI/2000-064/Tn

Abstract

The theoretical calculation of ISOPHOT point spread functions (PSF) and beam profiles is revisited. Numerical programs that include modeling of not only the primary and secondary mirrors, but also the telescope tripod were employed to calculate the PSF factors for the subinstruments PHT-P and PHT-C. The PSF factors for PHT-P, calculated with the new PSF model appear for the first time. The results are compared to the values from earlier reports and the ISOPHOT calibration tables. This leads to a clarification of the origin of various existing tables of PSF factors, the influence of source colour as well as a deeper understanding of the unexplained flux losses of the C200 array centred point source photometry. A successful adjustment of parameters also for the C100 model is proposed. Questions however arise about the way the effective solid angles for extended source photometry are calculated. Therefore values for several scenarios are given.

1 Introduction

The theoretical understanding of the energy distribution of a point source in the focal plane of the ISO telescope is very important for ISOPHOT, since its photometric calibration is based exclusively on point sources and the extended source calibration can only be performed indirectly. This energy distribution, with its integral over the infinite focal plane normalized to one, we call Point Spread Function (PSF). The diameter defined by the first minimum of the diffraction pattern around the central maximum is given approximately by the Airy-disk ($d_{Airy} = 0.839 \times \lambda$, with the wavelength λ in units of μm). For practical reasons we measure distances in the focal plane in arc seconds projected on the sky. One millimeter corresponds then to $22.92''$. At this point we also want to define the way in which we will use the term "beam profile". We understand it as the convolution of the PSF with the measuring aperture, which is either the field lens of the detector pixel of a C-array or the field aperture of a P-detector. Contrary to the PSF, the beam profile can be measured directly by performing a narrowly spaced raster map on a point source, covering also sufficient space outside the boundaries of the aperture.

Considerable work has been spent already on these topics by other authors. In particular the modelling of the PSF and the resulting theoretical beam profiles for ISOPHOT, first undertaken by Ackermann [1], have reached a high level of understanding after the theoretical modelling by Okumura [11], who included the telescope tripod into the PSF and the subsequent work by Herbstmeier [2], [3], modeling the ISOPHOT beam profiles. Since there were still some open questions

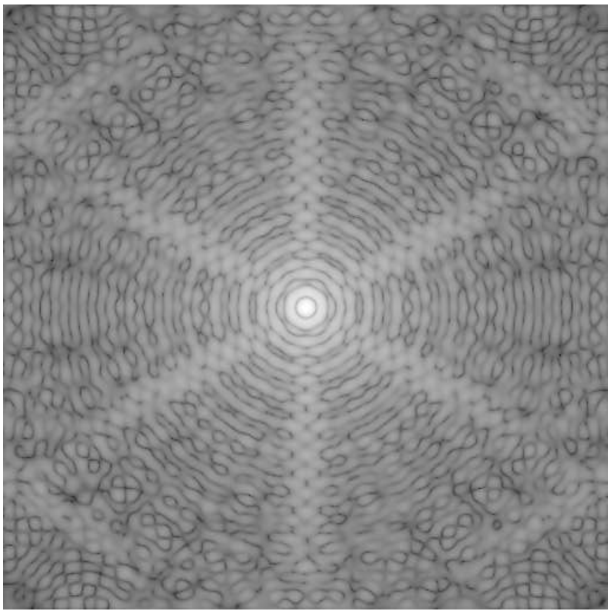

Figure 1: *The PSF calculated over an area of $5' \times 5'$ for a wavelength of 12 μm displayed with a logarithmic intensity scale to enhance the faint structure around the maximum. The sixfold symmetry results from the obscuration of the entrance aperture by the tripod.*

about the impact of the new PSF and the dependence on the source colour, and since not all PSF-factors necessary for photometry were calculated yet, the programs by Okumura and Herbstmeier were 'revived' by the author, checked and used to obtain the results presented here.

2 The Point Spread Function

For the numerical calculations Ackermann [1] initially approximated the PSF by a simple analytical telescope model, which takes into account the primary and the secondary-mirror. He used

$$PSF(v,\lambda) = \frac{\pi A}{\lambda^2 f^2} \frac{(J_1(v) - \epsilon J_1(\epsilon v))^2}{v^2},\ v = \frac{\pi\, r}{\lambda\, f}, \tag{1}$$

where $A = 0.282743$ m^2 is the unobscured telescope aperture, $f = 15$ stands for the f-ratio of the ISO telescope, r is the radial distance from the centre of the PSF in the focal plane, $\epsilon = 0.3$ describes the obscuration by the secondary mirror and J_1 is the first order Bessel function of the first kind.

Meanwhile a more accurate numerical model has been developed by Okumura for ISOCAM, which was used for ISOPHOT first in 1998. It incorporates the complete obscuration by the secondary mirror and the tripod. First a quasi punctate source of size 1 is transformed into Fourier space. There the result is multiplied by an image of the telescope aperture including the central obscurations of secondary and supporting tripod. The PSF is found by transforming the product back into the image plane. Finally the integral of the PSF is normalized such that,

$$\int^{\infty} PSF(\vec{r})d\vec{r} = 1, \tag{2}$$

where $\vec{r}$ is a location within the focal plane measured w.r.t. the aperture centre. We used for the telescope diameter 0.60 m, the central obscuration has a diameter of 0.174 m and the width of the tripod struts was set to 0.02 m.

An even newer model by Okumura [11], which incorporates also the shift due to the off-axis position of the instrument was not used, since a comparison of results at 200 and 25 μm yielded maximum differences of only 10^{-4} to 10^{-5} to the older model PSF, translating into changes in PSF correction factors of less than 1 %, but requiring about double the computation time.

PHT-P PSF Correction Factors (old model without tripod)

	PHT-P apertures												
λ	$5''$	$7.6''$	$10''$	$13.8''$	$18''$	$23''$	$20\times32''$	$52''$	$79''$	$99''$	$120''$	$127\times127''$	$180''$
P1													
3.29	0.88	0.91	0.94	0.95	0.97	**0.97**	0.97	0.99	0.99	0.99	0.99	1.00	1.00
3.6	0.84	0.91	0.93	0.95	0.96	**0.97**	0.97	0.99	0.99	0.99	0.99	0.99	1.00
4.8	0.70	0.90	0.90	0.93	0.95	**0.96**	0.96	0.98	0.99	0.99	0.99	0.99	0.99
7.3	–	0.77	0.89	0.90	0.92	**0.93**	0.94	0.97	0.98	0.99	0.99	0.99	0.99
7.7	–	0.74	0.88	0.90	0.91	**0.93**	0.94	0.97	0.98	0.98	0.99	0.99	0.99
10	–	–	0.75	0.88	0.90	0.91	0.92	**0.96**	0.97	0.98	0.98	0.99	0.99
11.3	–	–	0.70	0.82	0.90	0.90	0.91	**0.96**	0.97	0.98	0.98	0.98	0.99
12	–	–	0.69	0.78	0.90	0.90	0.91	**0.95**	0.97	0.98	0.98	0.98	0.99
12.8	–	–	0.68	0.75	0.89	0.90	0.91	**0.95**	0.97	0.97	0.98	0.98	0.99
15	–	–	–	0.69	0.84	0.90	0.89	**0.95**	0.96	0.97	0.97	0.98	0.98
P2													
20	–	–	–	–	0.70	0.78	0.82	0.92	**0.95**	0.96	0.97	0.97	0.98
25	–	–	–	–	–	0.69	0.77	0.90	**0.93**	0.95	0.96	0.96	0.97
P3													
60	–	–	–	–	–	–	–	0.69	0.85	0.90	0.90	0.91	**0.93**
100	–	–	–	–	–	–	–	–	0.68	0.71	0.81	0.87	**0.90**

Table 1: *PSF correction factors for PHT-P as calculated with the old analytical PSF model, as used until OLP9. The factors represent the intensity fraction of a point source entering an aperture of PHT-P. The numbers in bold print indicate the standard aperture/filter combinations.*

3 PSF Correction Factors

The ISOPHOT flux calibration was performed exclusively by using point sources. Since in general not all the flux is entering the detector due to the extension of the PSF, we define the PSF correction factor or short PSF factor f_{psf}. It is the fraction of the flux of a point source entering the aperture A of the detector, where it is positioned at the centre. The detector aperture is defined either by the rectangular field lens of a PHT-C detector or the round or rectangular field aperture of a P-detector. f_{psf} is calculated as the ratio between the integrals over the PSF within the aperture A and the integral over the entire focal plane. With the normalization of the PSF of equation (2), we get

$$f_{psf}(\vec{d},\lambda) = \frac{\int^{A} PSF(\vec{r}-\vec{d},\lambda)d\vec{r}}{\int^{\infty} PSF(\vec{r},\lambda)d\vec{r}} \stackrel{norm.}{=} \int^{A} PSF(\vec{r}-\vec{d},\lambda)d\vec{r}. \quad (3)$$

PHT-P PSF Correction Factors (monochromatic)

	PHT-P apertures												
λ	5″	7.6″	10″	13.8″	18″	23″	20×32″	52″	79″	99″	120″	127×127″	180″
P1													
3.29	0.84	0.88	0.91	0.92	0.94	**0.95**	0.96	0.99	1.00	1.00	1.00	1.00	1.00
3.6	0.82	0.87	0.90	0.92	0.94	**0.95**	0.96	0.98	1.00	1.00	1.00	1.00	1.00
4.8	0.68	0.86	0.87	0.90	0.92	**0.93**	0.94	0.97	0.99	0.99	1.00	1.00	1.00
7.3	0.65	0.76	0.86	0.86	0.89	**0.90**	0.91	0.96	0.97	0.98	0.99	0.99	1.00
7.7	0.64	0.72	0.84	0.86	0.88	**0.90**	0.91	0.95	0.97	0.98	0.99	0.99	1.00
10	0.54	0.66	0.72	0.84	0.86	0.87	0.89	**0.94**	0.96	0.97	0.98	0.98	0.99
11.3	0.54	0.65	0.68	0.79	0.86	0.87	0.88	**0.93**	0.95	0.96	0.97	0.98	0.99
12	0.44	0.65	0.67	0.76	0.86	0.87	0.88	**0.92**	0.95	0.96	0.97	0.98	0.99
12.8	0.36	0.65	0.66	0.72	0.86	0.86	0.87	**0.92**	0.94	0.96	0.97	0.97	0.98
15	0.36	0.60	0.65	0.67	0.82	0.86	0.86	**0.92**	0.94	0.95	0.96	0.97	0.98
P2													
20	0.19	0.54	0.60	0.65	0.68	0.76	0.79	0.89	**0.92**	0.94	0.94	0.95	0.97
25	0.15	0.36	0.54	0.60	0.65	0.67	0.75	0.87	**0.90**	0.92	0.93	0.94	0.96
P3													
60	0.04	0.15	0.15	0.19	0.36	0.44	0.52	0.66	0.82	0.86	0.87	0.88	**0.90**
100	0.04	0.04	0.04	0.15	0.15	0.19	0.26	0.60	0.65	0.68	0.77	0.85	**0.86**

Table 2: *PSF correction factors as calculated with the new numerical PSF model including the full central obscuration by the secondary and the tripod. The factors represent the intensity fraction of a point source entering an aperture of PHT-P. The numbers in bold print indicate the standard aperture/filter combinations.*

The offset $\vec{d}$ of the PSF centre w.r.t. the centre of the aperture was included to cover also the more general case of what is called a beam profile, i.e. the whole of the PSF factors for all positions of the point source relatively to the centre of the aperture. The standard PSF correction factor is generally calculated for a reference position that coincides with the centre of the detector pixel. $\vec{d}$ is zero then. Exceptions occur in special cases, like for the array centred position of C200.

For the normalization it is important to perform the numerical integration over the entire PSF out to a radius sufficiently distant from the centre, to reduce the systematic error. We chose the raster size for the PSF such that the ratio between the central value and the values at the border was of the order 10^{-6}. For the special wide field calculations described later this ratio was about 10^{-8}.

3.1 PSF Correction Factors for PHT-P

The PSF correction factors for ISOPHOT-P calculated with the analytical PSF for the flight model (FM) of ISOPHOT are found in the calibration Table `PPPSF.FITS` of OLP9. These deviate slightly from the factors published in the ISOPHOT Observer's Manual [6], which were derived for the parameters of the flight spare model (FS) of ISOPHOT, i.e. different reference wavelengths and different aperture diameters. The factors for the FM from the OLP9 calibration table are shown in Table 1.

In Table 2 the PSF correction factors calculated by the new numerical PSF calculation are shown. The results tend to be smaller by a few percent, i.e. more energy is falling outside of the central maximum due to diffraction by the tripod. These factors were still calculated monochromatically for

PHT-P PSF Correction Factors (broad band)

	PHT-P apertures												
λ	5″	7.6″	10″	13.8″	18″	23″	20×32″	52″	79″	99″	120″	127×127″	180″
P1													
3.29	0.85	0.88	0.91	0.92	0.95	**0.96**	0.96	0.99	0.99	0.99	1.00	1.00	1.00
3.6	0.81	0.88	0.91	0.92	0.94	**0.95**	0.96	0.98	0.99	0.99	1.00	1.00	1.00
4.8	0.69	0.86	0.88	0.90	0.92	**0.93**	0.94	0.98	0.99	0.99	0.99	0.99	1.00
7.3	0.64	0.76	0.85	0.87	0.89	**0.91**	0.92	0.96	0.97	0.98	0.99	0.99	0.99
7.7	0.64	0.73	0.85	0.87	0.88	**0.90**	0.91	0.96	0.97	0.98	0.99	0.99	0.99
10	0.54	0.66	0.73	0.84	0.87	0.88	0.89	**0.94**	0.96	0.97	0.98	0.98	0.99
11.3	0.48	0.66	0.68	0.79	0.86	0.87	0.89	**0.93**	0.96	0.97	0.97	0.98	0.99
12	0.48	0.65	0.70	0.78	0.86	0.87	0.88	**0.93**	0.95	0.97	0.97	0.98	0.99
12.8	0.42	0.65	0.66	0.73	0.86	0.87	0.88	**0.92**	0.95	0.96	0.97	0.98	0.98
15	0.33	0.61	0.66	0.67	0.80	0.86	0.85	**0.92**	0.94	0.95	0.96	0.97	0.98
P2													
20	0.22	0.47	0.59	0.65	0.69	0.75	0.79	0.89	**0.92**	0.93	0.95	0.95	0.97
25	0.17	0.41	0.54	0.63	0.66	0.70	0.76	0.88	**0.91**	0.93	0.94	0.95	0.96
P3													
60	0.04	0.09	0.15	0.23	0.36	0.46	0.51	0.68	0.81	0.86	0.87	0.88	**0.90**
100	0.01	0.04	0.05	0.09	0.15	0.22	0.27	0.59	0.66	0.70	0.77	0.83	**0.87**

Table 3: *PSF correction factors as calculated with the new numerical PSF model but also integrating over the instrumental spectral response, assuming a $\lambda F_\lambda = const.$ source colour.*

the reference wavelengths of the ISOPHOT filters, which are given in the first columns of Tables 1 and 2. To see the influence of the spectral width of the broad band filters, the PSF correction factors were calculated again (see Table 3), but this time also integrating over the instrument spectral response given by the spectral transmission of the filter and the relative spectral response of the detector.

$$f_{psf_{broadband}}(\vec{d}) = \frac{\int^{\infty} f_{psf}(\vec{d},\lambda)T(\lambda)F_\lambda(\lambda)d\lambda}{\int^{\infty} T(\lambda)F_\lambda(\lambda)d\lambda} \tag{4}$$

Since in this case we also need to assume a source colour, we adopted the reference spectrum F_λ that is used to express monochromatic flux densities for ISOPHOT. It fulfills $\lambda F_\lambda = const.$ or $\nu F_\nu = const.$ in frequency space. The results are tabulated in Table 3. A brief check was also made using a Rayleigh Jeans ($\lambda^4 F_\lambda = const.$) type source spectrum in the P_11.5 filter with the 52″ aperture, giving a difference of about 1/2 a per cent. Towards long wavelengths and small apertures the difference increases to a few per cent. This confirms the rather small dependence of the PSF on the source colour for PHT-P. This can also be seen from the comparison of monochromatic and broad band calculated PSF factors in Tables 2 and 3.

Theoretical PSF factors have also been calculated for the 3×3 and 2×2 detector arrays of the C-subsystem. The field lenses of 1.9×1.9 mm (43.548″) for C100 and 3.9×3.9 mm (89.388″) for C200 are taken as detector entrance apertures. In between the pixels there are gaps of 0.1 mm (2.3″). Given the dimensions of the Airy disk at the nominal wavelengths of 42″ to 88″ for C100 and 101″ to 168″ for C200, the PSF is just matching the pixel size, so it is not expected to see a flat plateau on top of a beam profile, as it would be the case for shorter wavelengths.

The PSF correction factors that were calculated initially with the analytical PSF model for a point source, centred on a pixel (f_{psf}^{pixel}), are listed in the second column of Table 4. These values were recalculated with the new numerical PSF for the reference wavelength of each filter and appear in column 3. To check the colour dependence of the fairly broad filters (spectral resolution 2-3) we also calculated the factors integrating over the filter bands, using both, a $\lambda F_\lambda = const.$ and a $\lambda^4 F_\lambda = const.$ source spectrum. The values are given in column 4 and 5 of Table 4.

PSF Correction Factors (design parameters)

filter	pixel centred				array centred			dev.
	old model	mono	broad band $\lambda F_\lambda = const.$	broad band $\lambda^4 F_\lambda = const.$	mono	broad band $\lambda F_\lambda = const.$	broad band $\lambda^4 F_\lambda = const.$	[%]
C_50	0.68	0.659	0.656	0.675	0.868	0.851	0.858	2.9
C_60	0.69	0.663	0.667	0.676	0.864	0.856	0.858	1.3
C_70	0.66	0.642	0.629	0.643	0.855	0.837	0.846	2.2
C_90	0.61	0.600	0.586	0.617	0.809	0.814	0.831	5.3
C_100	0.57	0.556	0.558	0.580	0.789	0.795	0.810	3.9
C_105	0.55	0.556	0.540	0.556	0.830	0.790	0.799	3.0
C_120	0.69	0.663	0.678	0.692	0.727	0.789	0.782	2.1
C_135	0.66	0.649	0.641	0.650	0.788	0.741	0.752	1.4
C_160	0.64	0.621	0.620	0.635	0.676	0.718	0.736	2.4
C_180	0.62	0.621	0.609	0.619	0.783	0.704	0.719	1.6
C_200	0.59	0.556	0.568	0.576	0.588	0.649	0.655	1.4

Table 4: *PSF correction factors calculated for all filter bands of PHT-C using standard design parameters for detector dimensions. Mono designates monochromatic calculation for the filter reference wavelengths. For the broad band calculation two different source spectra have been assumed. The deviation between both pixel centred values is given in the last column.*

In standard observations the point source is placed at the centre of the detector array. This is unfortunate in the case of C200, where the source is placed onto the narrow gap between the four pixels. To be less vulnerable to pointing errors and to achieve a better S/N, for point source photometry the calibrated fluxes of the four pixels are summed up, and, although there is no immediate need for C100 because it has a central pixel, the calibrated fluxes are also summed up for this array. The corresponding PSF factor describing the fraction of the flux of a point source that enters any of the pixels of the entire array we call f_{psf}^{array}.

We have calculated for all filters of C100 and C200 the PSF factors at the positions of a 3×3 grid placed over the central position and shifted by 1/2 a pixel respectively, such that in the case of C100 all pixel centres coincide with a raster position and for C200 the four corners coincide with the four pixel centres, while there are 4 positions in between 2 pixels each and one position at the centre of the array.

Both grids have a spacing of $d = 45.84''$, corresponding to the nominal distance between pixel centres or half this distance for C100 and C200 respectively. We confirmed that the small asymmetry between the y and z axis caused by the 6 fold diffraction pattern of the tripod is negligible, therefore we can assume equal characteristics of all pixels. We distinguish 3 important grid positions w.r.t. the centre of a pixel:

- the position at the nominal distance d along the coordinate axes at the centre of the next pixel.
- the position at a distance $d\sqrt{2}$, 45° diagonal to the spacecraft coordinate axes.

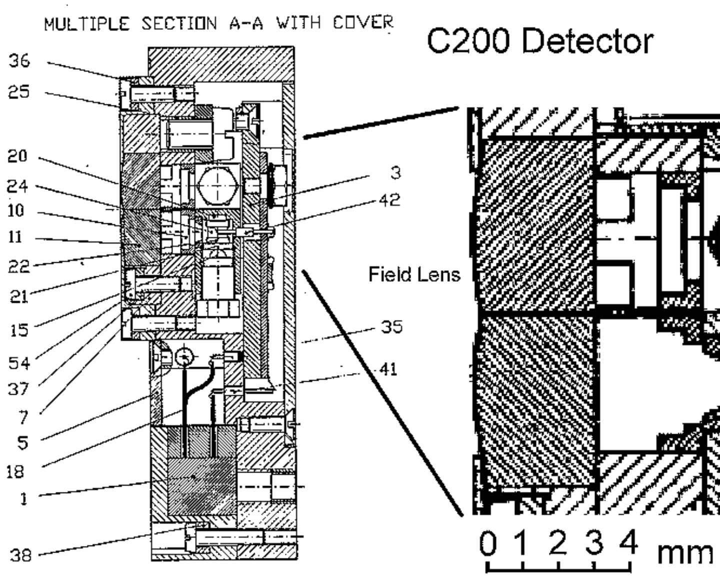

Figure 2: *Physical design of the C200 detector assembly seen from the side. Light enters from the left. The zoomed section on the right shows two detector pixels with their field lenses. The lower detector pixel is drawn cut-on, showing from left to right the field lens, the entrance cone and the detector crystal with its stressing mechanism.*

- the position at a distance of $d/2\sqrt{2}$ which for C200 is the array centre.

For C100 the array centred PSF factor is $f_{psf}^{array} = f_{psf}(0) + 4f_{psf}(d) + 4f_{psf}(d\sqrt{2})$. For C200 $f_{psf}^{array} = 4f_{psf}(d/2\sqrt{2})$ is calculated. The monochromatic values and the broad band values that include the integration over filter bands for both source colours are given in Table 4, columns 6 to 8. The last column shows the deviation between the broad band calculations for both source spectra. These reach 2.5 %, however may be much larger for steeper spectra.

3.2 Comparison to measured data

In orbit the PSF correction factors can not be determined directly. Our only "observable" is the ratio $f_{psf}^{pixel}/f_{psf}^{array}$, which can be used to estimate the quality of our model description. The comparison with the theoretical expectations is essentially a verification of the beam profile for a selected number of offset positions.

In Table 5 and 6 the second column shows the measured ratios, derived from the tables by Laureijs [8], who analyzed calibration observations of bright stars, asteroids and planets. The values were calculated as the ratio between the pixel centred PSF factors in Table 1 of [8] and the array centred PSF factors in Tables 4 and 9. To keep the influence of source colour low, we recalculated the theoretical values for a Rayleigh Jeans source spectrum of $\lambda^4 F_\lambda = const.$, matching better the colour of the observed sources. The theoretical ratio, calculated for the standard design parameters of the detectors, is given in the third column of Tables 5 and 6. A graphical representation is shown in Figures 3 and 4.

There are considerable deviations for C200 and moderate ones for C100. The data indicate a much stronger loss of flux at the central array position of C200 than expected. The flux received from the source at the centre of a pixel is even larger than the sum of the four fluxes measured when positioning the point source at the array centre.

4 Adjusting the Models for PHT-C

The discrepancy between model predictions and the actually measured ratios $f_{psf}^{pixel}/f_{psf}^{array}$ is quite strong for C200. Considering the detector design, which is illustrated in Figure 2, there are few parameters in the model, that are likely to influence this ratio:

- the true colour of the observed source,
- the actual geometrical size of the pixel aperture,
- the actual position of the pixel w.r.t. the array centre.

The influence of the source colour for sources with 'moderate' spectra is, as was shown, at the 2.5 % level and stays below current photometric accuracies.

For steeper spectra, however, it may be more and then represents a natural limit for the photometric accuracy, if not taken into account specifically. Note that this colour correction is in addition to the tabulated one that is applied within Interactive Analysis (PIA). In practise this correction is applicable only with a considerable computational effort and an a priori knowledge about the shape of the source SED.

C200: $f_{psf}^{pixel}/f_{psf}^{array}$

filter	measured	design parameters	pixel size $-9.4''$	pos. offset $+4.2''$
C_120	1.386 ± 0.078	0.885	1.384	1.336
C_135	1.162 ± 0.059	0.865	1.229	1.184
C_160	1.212 ± 0.048	0.863	1.221	1.153
C_180	1.013 ± 0.076	0.861	1.161	1.111
C_200	0.851 ± 0.025	0.880	1.103	1.113

Table 5: *Measured and theoretical ratios between the flux of a point source positioned at a pixel centre and at the array centre of C200 with the fluxes of all detectors added. All ratios are calculated for a Rayleigh Jeans source spectrum.*

The actual geometrical size of the pixels may plausibly be smaller than the design values used so far, considering the array design (see Figure 2) and the fact that $5''$ correspond to only 0.22 mm in the focal plane. During some - but time consuming - test calculations, ratios were obtained, that are much closer to the measured ones. The best results found during these tests for apertures of $80'' \times 80''$ and $85'' \times 85''$ are shown in Table 5 in columns 2 and 3. Again, to stay closer to the conditions of the observations, a Rayleigh Jeans source colour was assumed in the broad band calculations.

Comparing theoretical and measured beam profiles in the filters C_120 and C_200, Herbstmeier [3] found absolute deviations of pixel centres of $6''$ in y-direction and $8''$ in z-direction. A test calculation with each pixel displaced by about $4''$ away from the array centre along both coordinate axes (see

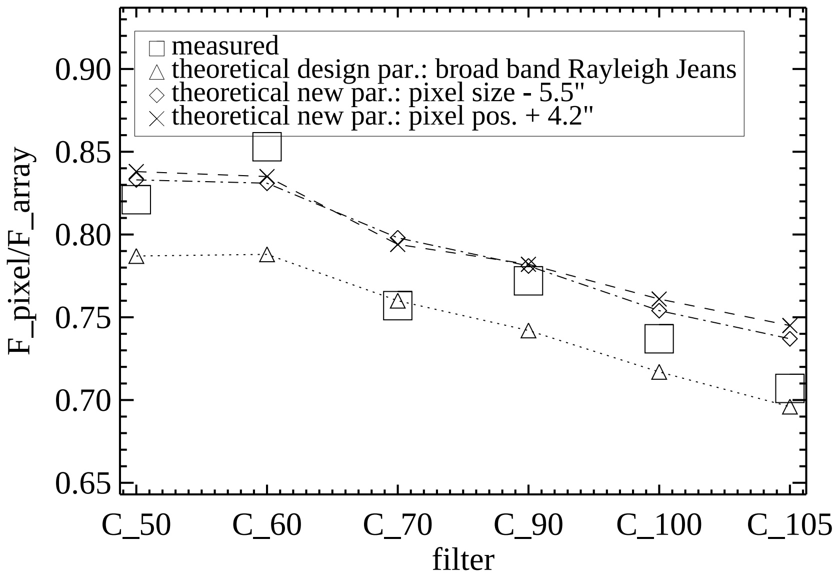

Figure 3: *Diagram of measured and theoretical ratios between the flux of a point source positioned at a pixel centre and at the array centre of C100 with the fluxes of all detectors added.*

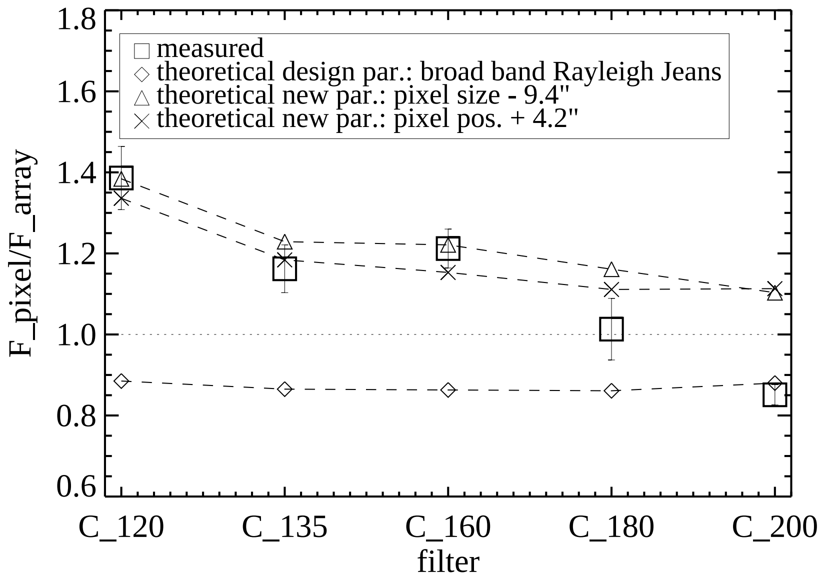

Figure 4: *Diagram of measured and theoretical ratios between the flux of a point source positioned at a pixel centre and at the array centre of C200 with the fluxes of all detectors added.*

column 5 of Table 5) gave a reasonable match too and showed how critical the distance of the four pixels to the array centre is. A small displacement of the pixel centres must therefore also be considered as a possible explanation.

Apparently both methods, reduction of pixel size and increase of pixel distance to array centre yield better consistency of the theoretical calculations and the observations, as seen in Figure 4. We also see that for the two longest wavelength filters there is a drop-off of the measurements w.r.t. the theory, indicating more flux entering the detectors from an array centred source than expected from the revised model. Without any further modeling of the instrument optics, including diffraction, we can only speculate that with increasing wavelength the effective pixel aperture increases again due to diffraction effects.

C100: $f_{psf}^{pixel}/f_{psf}^{array}$

filter	measured	design parameters	pixel size $-5.5''$	pos. offset $+4.2''$
C_50	0.821 ± 0.006	0.787	0.833	0.838
C_60	0.853 ± 0.004	0.788	0.831	0.835
C_70	0.757 ± 0.006	0.760	0.798	0.794
C_90	0.772 ± 0.008	0.742	0.781	0.782
C_100	0.737 ± 0.008	0.717	0.754	0.761
C_105	0.707 ± 0.009	0.696	0.737	0.745

Table 6: *Measured and theoretical ratios between the flux of a point source positioned at a pixel centre and at the array centre of C100 with the fluxes of all detectors added. All ratios are calculated for a Rayleigh Jeans source spectrum.*

For C100, although the difference between measurements and theory is not as dramatic, we show again two solutions, one changing pixel size and one changing pixel position (see Table 6 and Figure 3). Also mixed solutions with changes of both parameters were tried but did not lead to any significant improvements. It should be noted that all results were found by performing a series of monochromatic calculations and then a broad band calculation for each of the best solutions for confirmation. No automatic fitting in a least squares sense was used due to the huge computational effort. In Table 7 and 8 we show a summary of the PSF correction factors that would apply if any

C100: Adjusted PSF Correction Factors

	reduced pixel size			shifted pixel pos.		
filter	centre	dist. d	dist. $d\sqrt{2}$	centre	dist. d	dist. $d\sqrt{2}$
C_50	0.633	0.029	0.007	0.656	0.039	0.010
C_60	0.652	0.031	0.005	0.667	0.039	0.008
C_70	0.596	0.030	0.010	0.629	0.038	0.014
C_90	0.537	0.028	0.014	0.586	0.038	0.019
C_100	0.498	0.027	0.017	0.558	0.038	0.021
C_105	0.475	0.027	0.018	0.540	0.040	0.022

Table 7: *PSF correction factors calculated for all filter bands of C100. The calculations were done including the broad band spectral transmissions of the instrument assuming a $\lambda F_\lambda = const.$ source spectrum. The factors were calculated for both model solutions, i) with the pixel size set to $38''$ and ii) with the pixel centres at distances d of $50''$.*

C200: Adjusted PSF Correction Factors

filter	reduced pixel size centre	dist. d	dist. $d\sqrt{2}$	dist. $d/2\sqrt{2}$	shifted pixel pos. centre	dist. d	dist. $d\sqrt{2}$	dist. $d/2\sqrt{2}$
C_120	0.663	0.033	0.006	0.125	0.678	0.041	0.009	0.197
C_135	0.619	0.033	0.010	0.128	0.641	0.039	0.014	0.185
C_160	0.590	0.032	0.014	0.124	0.620	0.039	0.017	0.180
C_180	0.574	0.031	0.016	0.125	0.609	0.039	0.020	0.176
C_200	0.524	0.030	0.019	0.120	0.568	0.040	0.022	0.162

Table 8: *PSF correction factors calculated for all filter bands of C200 The calculations were done including the broad band spectral transmissions of the instrument assuming a $\lambda F_\lambda = const.$ source spectrum. The factors were calculated for both model solutions, i) with the pixel size set to* $80''$ *and ii) with adjacent pixel centres at distances d of* $100''$.

of the solutions would be adopted.

4.1 Fitting to measured Beam Profile

To clarify if there was actually a different pixel size or rather a change in pixel position, we checked a data set measured with C200 in the C_120 filter on the planetary nebula NGC7027, which is considered point like at these wavelengths. A 17×17 raster was performed around the source centre in steps of $22''$ with the raster legs aligned with the spacecraft y-axis. The data set has already been analyzed by [4]. The corresponding TDT number is 4504201.

We processed the data with PIA V9.0.1(e) in a standard way to AAP level. From here we used special IDL routines to fit 2 dimensional model beam profiles, one calculated for standard design parameters and the other with a reduced pixel size to $80''$. The results are shown in Figure 5 as contour plots.

The fits are generally very good, however, the contours of the model with standard pixel size match better to the data than the one with reduced pixel size.

C200: Distances between pixels

	pixel 89.4″ dist.	dev.	pixel 80″ dist.	dev.	(Héraudeau et al. 97) dev.
pixel 1-2	96.49	4.81	95.17	3.49	4.63
pixel 2-3	98.29	6.61	97.93	6.25	7.11
pixel 3-4	92.51	0.83	91.75	0.07	0.24
pixel 4-1	105.75	14.07	105.30	13.62	12.25

Table 9: *The distances in* $''$ *between the detector pixels of C200 parallel to the coordinate axes and the deviation from the nominal distance* $91.68''$. *The centres found show little dependence on the pixel size of the model and are very consistent with the results of Héraudeau et al. [4], who fitted a gaussian beam profile.*

From the positions of the fitted pixel centres the relative distances parallel to the coordinate axes were calculated and their deviation from the design value of $91.68''$. These are shown in Table 9 together with the corresponding deviations calculated from the numbers given in [4], who fitted 2 dimensional gaussians.

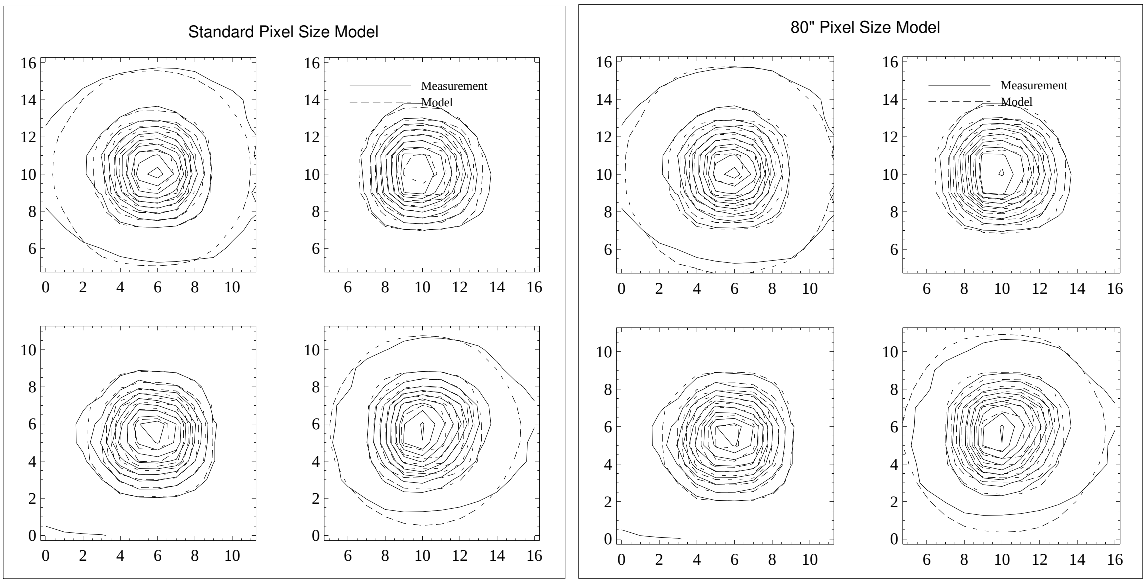

Figure 5: *Contour plots of measured beam profiles and fitted models. The measurements were performed in the C_120 filter on the planetary nebula NGC7027, which is considered to be point like at this wavelength. The spatial scales are in units of arc minutes originating at an arbitrary position. The spacecraft y-axis goes from right to left and the z-axis from bottom to top. The four pixels are plotted in separate diagrams since otherwise the beam profiles would overlap.*

The distances and deviations found for the two different models are very consistent with each other and with the values found by [4]. Only little dependence on the model profile is found. The distances are all larger than the design value by up to 14″. We therefore conclude that the different ratios of PSF factors of single pixel and array are rather due to inaccuracies in the center positions of the pixels than due to smaller effective collecting areas. Given that the deviations vary strongly, in order to improve the understanding further, one would need to extend the modelling to asymmetric cases.

5 Solid Angles

To express observations of extended sources in terms of surface brightness, the beam size projected onto the sky is needed. The measurement is then expressed in MJy/sr. Strictly this unit is defined for an infinitely extended source only. Interpreting an extended source as the sum of an infinite amount of point sources spread over the sky, the effective solid angle Ω can be understood as the beam profile integrated over the entire sky.

$$\Omega(\lambda, A) = \int^{\infty} f_{psf}(\vec{d}, \lambda) d\vec{d} \tag{5}$$

In practise we calculated the beam profiles as data arrays with horizontal spacings of typically 5″ between raster points, so Ω is derived without sophistication as the total of the entire array, times the corresponding area on the sky for one raster element in steradian.

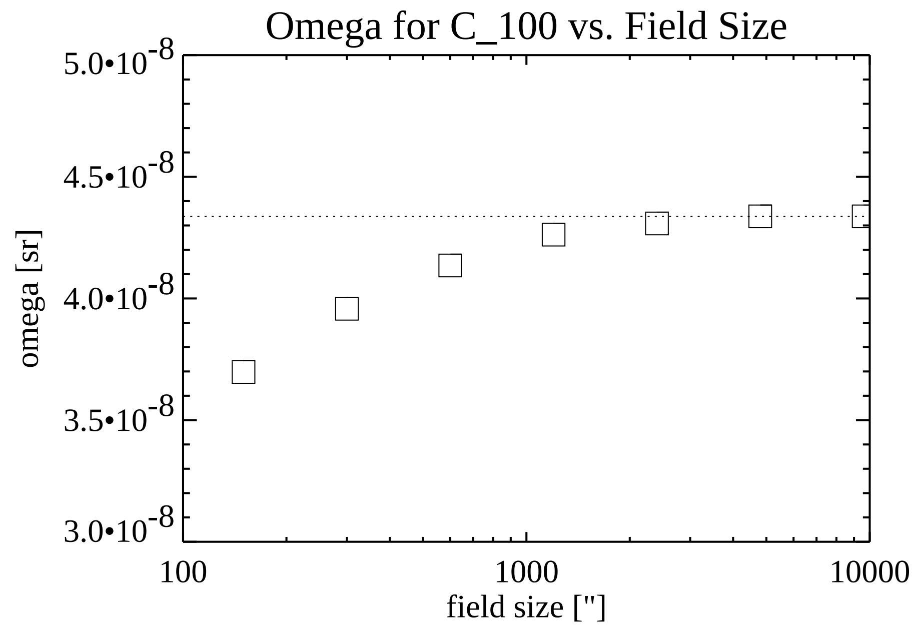

Figure 6: *Curve of growth, showing the integrated solid angle at 100 μm over arrays of different sizes between 150 and* 9600″. *The dotted line is the estimated asymptote.*

The difficulty in our numeric calculations is again to integrate far enough towards ∞, to keep the remainder negligible. To learn about the limitations, a curve of growth was calculated, extending the array size from 150″ to 9600″. The result is plotted in Figure 6. To achieve accuracies at the 2 % level, field sizes of 1/2 a degree are necessary. It should be noted that extending the area, where the PSF is calculated, which of course should at least match the area of the beam profile, did not change the curve recognizably.

5.1 Solid angles for PHT-C

First we calculated the beam profiles of the C-detectors, which were assumed to be most critical because of the wide PSF at long wavelengths. Because of the computation times involved we stayed with the monochromatic model. To save more time, the integration of the beam profile was split into a central area of 800″, that was calculated with 5″ spacing and a much wider area of 200′, that was sampled in 133″ steps, so that the central 6×6 array could be directly replaced by the integral over the smaller array with the finer sampling. The individual results of the central and far-range arrays and their sum are given in Table 10.

It turned out that the derived solid angles did not match the numbers calculated by Herbstmeier [2] [3], but needed to be divided by the PSF factor to yield the same numbers. This was thoroughly verified for the C_100 filter, i.e. renormalizing the beam profiles to their peak value before the integration.

For the time being, the motivation for this remains unclear. The nominal pixel sizes projected onto the sky of 43.548″ and 89.388″ yield geometrical solid angles of 4.457×10^{-8} sr and 1.878×10^{-7} sr, which are very close to the derived values (see Table 10 column 4) that are based on the

PHT-C Solid Angles (design parameters)

filter	800″ array	200′ array	total	total / F_{psf}
		[steradian]		
C_50	4.610e-08	4.377e-10	4.654e-08	7.067e-08
C_60	4.441e-08	3.708e-10	4.478e-08	6.733e-08
C_70	4.580e-08	4.689e-10	4.627e-08	7.289e-08
C_90	4.129e-08	4.349e-10	4.172e-08	7.075e-08
C_100	4.195e-08	4.791e-10	4.242e-08	7.629e-08
C_105	4.613e-08	6.293e-10	4.676e-08	8.407e-08
C_120	1.731e-07	2.534e-09	1.756e-07	2.637e-07
C_135	1.811e-07	3.637e-09	1.847e-07	2.848e-07
C_160	1.696e-07	3.979e-09	1.736e-07	2.797e-07
C_180	1.895e-07	4.719e-09	1.942e-07	3.130e-07
C_200	1.614e-07	4.557e-09	1.660e-07	2.985e-07

Table 10: *Solid angles derived from integrated beam profiles for different PHT-C filters. The second column shows the integrals of the narrowly spaced central section, while the third column shows the integral over the surrounding sparsely sampled area. The fourth and fifth column show the sum of the previous two and this sum divided by the PSF factor.*

PHT-C Solid Angles (adjusted apertures)

filter	800″ array	200′ array	total	total / F_{psf}
		[steradian]		
C_50	3.529e-08	3.366e-10	3.563e-08	5.509e-08
C_60	3.457e-08	2.880e-10	3.486e-08	5.341e-08
C_70	3.280e-08	3.356e-10	3.313e-08	5.630e-08
C_90	3.412e-08	3.583e-10	3.448e-08	6.200e-08
C_100	3.398e-08	3.880e-10	3.436e-08	6.829e-08
C_105	2.955e-08	4.022e-10	2.995e-08	6.702e-08
C_120	1.530e-07	2.240e-09	1.553e-07	2.357e-07
C_135	1.330e-07	2.668e-09	1.357e-07	2.187e-07
C_160	1.425e-07	3.346e-09	1.458e-07	2.439e-07
C_180	1.316e-07	3.270e-09	1.349e-07	2.426e-07
C_200	1.308e-07	3.693e-09	1.345e-07	2.626e-07

Table 11: *Solid angles derived from integrated beam profiles for different PHT-C filters, assuming the adjusted solid angles that match the measured ratios $f_{psf}^{pixel}/f_{psf}^{array}$. The second column shows the integrals of the narrowly spaced central section, while the third column shows the integral over the surrounding sparsely sampled area. The fourth and fifth column show the sum of the previous two and this sum divided by the PSF factor respectively.*

normalization of the integrated point source to 1 (see Equation 2).

Looking at the limit for small wavelengths, both values become the same because the beam profile becomes rectangular and one within the geometrical boundaries of the aperture. The other extreme, going to longer wavelengths, is less clear.

To complete the set of numbers given here, we have also calculated the solid angles under the assumption that the smaller adjusted aperture diameters that match the measured ratios $f_{psf}^{pixel}/f_{psf}^{array}$ apply. Table 11 shows the values. Again we also give the numbers for a re-normalized beam profile to its peak.

5.2 Solid angles for PHT-P

The PHT-P solid angles were calculated in a much simpler way, mostly directed by the amount of computation time necessary to calculate all combinations of aperture and filter of the P-subinstrument. The beam profiles were calculated as arrays of 61×61 elements with field sizes of $50''$ for all apertures below $23''$ diameter and $240''$ for the bigger ones. It is clear that the systematic errors, in particular for the larger apertures close to the limited array size, are still large, however given the already considerable qualitative differences found between measured and theoretical beam profiles by Müller [10], a larger effort seemed not to be justified. The results are presented in Tables 12 and 13

PHT-P solid angles [10^{-7} sterad]

	PHT-P apertures												
λ	$5''$	$7.6''$	$10''$	$13.8''$	$18''$	$23''$	$20\times32''$	$52''$	$79''$	$99''$	$120''$	$127\times127''$	$180''$
P1													
3.29	0.0039	0.0124	0.0210	0.0344	0.0641	**0.0958**	0.1373	0.5125	1.1114	1.7933	2.6260	3.7295	5.9692
3.6	0.0039	0.0122	0.0210	0.0346	0.0641	**0.0955**	0.1361	0.5114	1.1119	1.7936	2.6261	3.7292	5.9704
4.8	0.0038	0.0120	0.0211	0.0342	0.0642	**0.0947**	0.1358	0.5132	1.1156	1.7935	2.6279	3.7636	5.9669
7.3	0.0040	0.0121	0.0206	0.0333	0.0626	**0.0927**	0.1322	0.5128	1.1188	1.7961	2.6232	3.7408	5.9557
7.7	0.0036	0.0118	0.0204	0.0335	0.0620	**0.0930**	0.1331	0.5120	1.1213	1.7958	2.6223	3.7063	5.9531
10	0.0035	0.0124	0.0198	0.0338	0.0612	0.0900	0.1287	**0.5124**	1.1216	1.7937	2.6132	3.7394	5.9334
11.3	0.0044	0.0108	0.0201	0.0322	0.0605	0.0908	0.1317	**0.5138**	1.1170	1.7852	2.6101	3.7232	5.9184
12	0.0037	0.0121	0.0205	0.0318	0.0594	0.0908	0.1248	**0.5136**	1.1182	1.7862	2.6071	3.6934	5.9159
12.8	0.0032	0.0119	0.0200	0.0319	0.0592	0.0895	0.1246	**0.5107**	1.1154	1.7851	2.6017	3.7295	5.9111
15	0.0043	0.0114	0.0186	0.0318	0.0632	0.0912	0.1279	**0.5078**	1.1111	1.7662	2.5926	3.7028	5.8846
P2													
20	0.0031	0.0131	0.0199	0.0323	0.0601	0.0848	0.1218	0.5096	**1.0946**	1.7637	2.5621	3.6138	5.8151
25	0.0038	0.0114	0.0199	0.0304	0.0579	0.0842	0.1263	0.5076	**1.0926**	1.7446	2.5439	3.6551	5.7880
P3													
60	0.0043	0.0172	0.0172	0.0215	0.0518	0.0692	0.1029	0.4638	1.0249	1.6943	2.4302	3.3163	**5.4348**
100	0.0105	0.0105	0.0105	0.0404	0.0404	0.0496	0.0757	0.4943	1.0640	1.5572	2.2801	3.4542	**5.2708**

Table 12: *The solid angles of the PHT-P subinstrument calculated as the integral over the beam profile at the filter reference wavelength.*

PHT-P solid angles / f_psf [10^{-7} sterad]

	PHT-P apertures												
λ	$5''$	$7.6''$	$10''$	$13.8''$	$18''$	$23''$	$20\times32''$	$52''$	$79''$	$99''$	$120''$	$127\times127''$	$180''$
P1													
3.29	0.0046	0.0140	0.0231	0.0681	0.0681	**0.1005**	0.1428	0.5192	1.1137	1.7933	2.6260	3.7295	5.9691
3.6	0.0048	0.0139	0.0234	0.0683	0.0683	**0.1007**	0.1423	0.5194	1.1172	1.7940	2.6261	3.7292	5.9703
4.8	0.0054	0.0140	0.0241	0.0698	0.0698	**0.1014**	0.1444	0.5264	1.1294	1.8049	2.6309	3.7635	5.9668
7.3	0.0061	0.0160	0.0241	0.0704	0.0704	**0.1023**	0.1448	0.5367	1.1496	1.8288	2.6554	3.7703	5.9635
7.7	0.0057	0.0161	0.0242	0.0704	0.0704	**0.1032**	0.1463	0.5370	1.1551	1.8316	2.6589	3.7420	5.9678
10	0.0065	0.0185	0.0271	0.0708	0.0708	0.1027	0.1447	**0.5458**	1.1702	1.8500	2.6727	3.8044	5.9920
11.3	0.0081	0.0166	0.0285	0.0703	0.0703	0.1044	0.1491	**0.5513**	1.1713	1.8509	2.6839	3.8036	5.9962
12	0.0085	0.0186	0.0296	0.0692	0.0692	0.1049	0.1421	**0.5543**	1.1785	1.8585	2.6881	3.7822	6.0038
12.8	0.0087	0.0182	0.0298	0.0692	0.0692	0.1037	0.1426	**0.5532**	1.1795	1.8632	2.6899	3.8294	6.0096
15	0.0119	0.0191	0.0287	0.0767	0.0767	0.1062	0.1488	**0.5538**	1.1847	1.8603	2.7020	3.8293	6.0164
P2													
20	0.0162	0.0244	0.0332	0.0852	0.0852	0.1120	0.1538	0.5701	**1.1903**	1.8856	2.7132	3.7934	6.0193
25	0.0253	0.0315	0.0371	0.0885	0.0885	0.1215	0.1679	0.5818	**1.2074**	1.8961	2.7233	3.8809	6.0580
P3													
60	0.0962	0.1146	0.1146	0.1431	0.1431	0.1590	0.1991	0.6839	1.2448	1.9686	2.8013	3.7746	**6.0308**
100	0.2357	0.2357	0.2357	0.2700	0.2700	0.2569	0.2962	0.8257	1.6075	2.1939	2.9445	4.0845	**6.1044**

Table 13: *The solid angles of the PHT-P subinstrument calculated as the integral over the beam profile at the filter reference wavelength, divided by the PSF factor.*

6 Conclusions

We have investigated the modeling of ISOPHOT point spread functions and beam profiles, using numerical computations that include not only the primary and secondary mirrors of the telescope, but also the support structure of the secondary. The PSF factors of PHT-P were recalculated monochromatically for the reference wavelength of the filter as well as integrating over the spectral profile, assuming a certain source spectrum. The colour dependence stays below a per cent, however differences between the previous analytical PSF model and the new one are up to 5 per cent.

The PSF factors calculated for the C-arrays confirm the values derived earlier in [2] and [3]. Comparing the ratios between array centred and pixel centred factors to actually measured ratios [8] shows a large discrepancy for C200 and a moderate one for C100. However, it could be demonstrated that adjusting either pixel size or pixel position by small amounts brings the model predictions for C200 within the errors except for the C_200 filter, and for C100 within ± 5 per cent of the measurements. Considering the photometric accuracy of C100, the match is quite good.

A fit of the models to measurements in the C_120 filter indicates that the discrepancy for the C200 array is rather due to larger distances between pixels than due to smaller effective areas of the pixels.

The calculation of the solid angles appeared straight forward on first sight, however there is a disagreement with previous calculations in [3]. Generally the previous values for the C-group could be confirmed, but only if the beam profile is re-normalized to its maximum. The difference is directly proportional to the respective PSF factor and is negligible at shorter wavelengths, but quite strong at the 40 % level at 200 μm. The values derived here are rather close to the geometrical projection of the aperture onto the sky. We argue that there is no good reason to re-normalize to the maximum and that a significant correction of the solid angles is necessary, but have to postpone the proof to a later stage. The same difference occurs for the P-group, however much less pronounced. Again most of our values are close to the geometrical solid angles.

Apart from this correction, the newly derived solid angles are slightly higher than the matching older ones [3] for the C-arrays, probably due to the two resolution approach used in the calculation, which results in a better coverage of the wings of the PSF out to $100''$.

Acknowledgements

The author thanks R. Laureijs, K. Okumura and T. Müller for enlightning discussions and U. Klaas for supplying the original PSF-factors calculated with the program of Ackermann. Further U. Herbstmeier and K. Okumura are acknowledged for supplying their source code.

References

[1] Ackermann, E. 1990, Diploma thesis, MPI für Astronomie, Heidelberg

[2] Herbstmeier, U. 1998, "ISOPHOT Footprints C100-Comparison between modelled and measured footprints - the derived parameters", internal report

[3] Herbstmeier, U. 1998, "ISOPHOT Footprints C200-Comparison between modelled and measured footprints - the derived parameters", internal report

[4] Héraudeau, Ph., Surace, C., Herbstmeier, U. 1997, "Report on beam profiles measurement of the ISOPHOT C100 and C200 detector arrays" MPIA internal report

[5] Kessler, M.F., Steinz, J.A., Anderegg, M.E., et al. 1996, A&A, 315, L27

[6] ISOPHOT Observer's Manual, Version 3.1, Klaas, U., Krüger, H., Heinrichsen, I., Heske, A., Laureijs, R. ed. 1994

[7] Klaas, U., Lemke, D., Kranz, T., Laureijs, R.J., Leinert, C., Schubert, J., Stickel, M., Toth, L.V. 1998, Proc. SPIE 3354-111

[8] Laureijs, R. 1999, "Point spread function fractions related to the ISOPHOT C100 and C200 arrays", IDC technical report

[9] Lemke, D., Klaas, U., et al. 1996, A&A, 315, L64

[10] Müller, T.G. 2000, Proc. of "ISO Beyond Point Sources: Studies of Extended Infrared Emission", Madrid, Spain, 14-17 Sep 1999 (ESA SP-455)

[11] Okumura, K. 2000, Proc. of "ISO Beyond Point Sources: Studies of Extended Infrared Emission", Madrid, Spain, 14-17 Sep 1999 (ESA SP-455)